MOF-modified polyester fabric coated with reduced graphene oxide/polypyrrole as electrode for flexible supercapacitors

Marjan Barakzehi[a, b], Majid Montazer [a,*], Farhad Sharif [c], Truls Norby[b], Athanasios Chatzitakis[b]

[a] Department of Textile Engineering, Functional Fibrous Structures & Environmental Enhancement (FFSEE), Amirkabir Nanotechnology Research Institute, Amirkabir University of Technology, Hafez Ave. No-424, Tehran, Iran

[b] Centre for Materials Science and Nanotechnology, Department of Chemistry, University of Oslo, FERMiO, Gaustadalléen 21, No-0349, Oslo, Norway

[c] Department of Polymer Engineering and Color Technology, Amirkabir University of Technology, Hafez Ave. No-424 Tehran, Iran

---

* Corresponding author.

E-mail address: tex5mm@aut.ac.ir (M. Montazer).

12   Abstract

13   The interest in wearable supercapacitors has been flourishing in both the scientific

14   and industrial fields. Here, daily-used polyester fabric (PET) is modified by using

15   an Al-based MOF, namely MIL-53(Al), via a layer-by-layer assembly method at

16   room temperature. Then, reduced graphene oxide is deposited on the PET/MOF

17   surface through dip coating in a graphene oxide suspension, followed by chemical

18   reduction. Ultimately, pyrrole is polymerized on the surface of the PET/MOF/rGO

19   surface by an *in situ* chemical polymerization process. The obtained composite is

20   used as electrode achieving an areal capacitance of 510 mF cm^{-2} at a scanning rate

21   of 1 mV s^{-1} in an aqueous H_2SO_4 electrolyte. The optimized electrode is employed

22   in a symmetrical solid-state-supercapacitor device, which delivers a volumetric

23   capacitance of 3.5 F cm^{-3}, energy density of 64 µW h cm^{-3} and power density of 0.6

24   mW cm^{-3}. The symmetrical device shows a good cycling stability even after 12

25   months storage in ambient conditions retained 85% of the initial capacitance after

26   1000 voltammetric cycles.

27   Keywords: wearable supercapacitor, metal-organic framework, polyester fabric,

28   reduced graphene oxide/polypyrrole composite.

1. Introduction

Supercapacitors can be integrated with textiles of smart garments in order to power electronic devices [1,2]. In this, one takes advantage of the textiles in terms of their mechanical strength, flexibility, low cost, light weight, safety, easy handling and breathability together with the general advantages of supercapacitors, such as high power density, long-term cycling lifetime and fast charge-discharge rates [3-6].

Lately, Metal Organic Frameworks (MOFs) have drawn extensive attention as potential materials in energy storage applications due to their ultra-high surface area, versatility, tailored properties, and their ability to combine pseudocapacitive redox metal centers [7-9]. Moreover, MOFs' organic linkers can contribute to the Electrical Double Layer Capacitance (EDLC). Generally, in supercapacitor applications, three categories of MOFs are exploited, namely the pristine MOFs and the MOFs pyrolyzed under inert and ambient atmospheres [10,11].

The pristine MOFs usually suffer from low conductivity due to the presence of insulating ligands in their structures. In addition, the participation of the d-orbitals of the metal ions in the coordination bonds does not allow the electron delocalization across the framework [12-14]. Therefore, electronically conductive materials must be incorporated with the MOF in order to increase their conductivity. Intercalation of conjugated polymers such as polypyrrole (PPy),

polyaniline (PANI) and poly(3,4-ethylenedioxythiophene) (PEDOT) is frequently reported as an effective method to enhance the electrical conductivity of the pristine MOFs. The intercalation of the conducting polymers (CPs) not only boosts the charge conduction properties, but also improves the faradaic processes at the interface of electrode/electrolyte [13,15-18]. Wang *et al.* proposed a strategy to interweave PANI into MOF crystals in order to synthesize a conductive porous electrode. Firstly, ZIF-67 was deposited on a carbon cloth with the aid of a binder and then PANI was electrodeposited. Such an electrode and the resulting supercapacitor device yielded areal capacitances reported to be 2146 mF cm^{-2} at 10 mV s^{-1} and 35 mF cm^{-2} at 0.05 mA cm^{-2} [15].

However, CPs tend to swell during the doping/de-doping process, a fact that limits the cycleability of the supercapacitor devices. Hence, CPs are combined with carbonaceous materials such as reduced graphene oxide (rGO) to improve their stability. In fact, graphene sheets with high surface area result in high interfacial EDLC and they can provide a stable framework for the polymer deposition, which is able to buffer the volume change of the polymer [19]. We have recently developed an rGO/PPy composite coated on polyester (PET) fabric obtaining an electronic conductivity of 0.81 S m^{-1}, and the all-solid-state supercapacitor delivers an areal capacitance of 0.23 F cm^{-2} at 1 mV s^{-1}. It also retains about 76% of the initial capacitance after 6000 voltammetric cycles (VCs) [20]. Fu *et al*. prepared a

70 flexible supercapacitor based on MOF/graphene oxide onto a carbon nanotube film

71 in which PEDOT was further electrochemically deposited. Such a device offered

72 an areal capacitance of 38 mF cm^{-2} at 5 mV s^{-1} and a capacitive retention of 89%

73 after 2000 VCs [21].

74 MIL-53(Al) (MIL, Matérial Institut Lavoisier) is one of the most stable MOFs in

75 acidic conditions and elevated temperatures, comprised of interconnected chains of

76 corner sharing $AlO_4(OH)_2$ octahedra linked by terephthalic acid (TPA) [22]. It is

77 conventionally synthesized under hydrothermal conditions (220 °C for 3 days) and

78 a further thermal activation step (330 °C for 3 days) is required in order to remove

79 protonated TPA molecules trapped within the structural pores.

80 Here, we aim to prepare MIL-53(Al) particles directly on the PET fabric without

81 the assistance of any binder. Although the high thermal stability of the MOFs

82 allows the thermal treatment of the material, the underlying thermoplastic PET

83 substrate does not tolerate such temperatures. PET begins to soften beyond its glass

84 transition temperature (T_g) at 70 °C until its complete melting at around 260 °C.

85 Sánchez-Sánchez *et al*. reported an innovative way to synthesize MIL-53(Al) at

86 room temperature (RT) by using organic salts instead of the analogous protonated

87 ligand. Since the alkaline-based salts of the TPA ligand are perfectly soluble in

88 water in RT, the severe conditions of the conventional procedure for the PET

89   substrate can be avoided. Furthermore, the synthesized MIL-53 has some

90   additional advantages such as the nano-crystalline nature and the reduced amount

91   of protonated ligand filling of the MOF pores [23]. In addition, Haque *et al*.

92   proposed a MOF purification method based on ultrasonic treatment in the presence

93   of *N,N*-dimethylformamide (DMF) at mild temperatures (70 °C) which can

94   effectively remove the uncoordinated and free carboxylic acids from the pores

95   [24].

96   In this work, we describe a facile method for the synthesis of flexible, binder-free

97   electrodes and the subsequent supercapacitor device by designing a novel ternary

98   composite coating on the polyester fabric. Firstly, and in order to introduce more

99   porosity to the fabric surface and benefit from the MOF's contribution to the total

100 capacitance, aluminum terephthalate ($Al_2(BDC)_3$) MOF particles are grown on the

101 PET surface by one or six cycles of layer-by-layer deposition. Secondly, GO is

102 embedded on the PET/MOF-x and is further chemically reduced to rGO. Finally,

103 pyrrole is polymerized *in situ* on the PET/MOF-x/rGO composite. The chemical

104 and morphological properties of the PET/MOF-x/rGO/PPy (x=1 or 6) electrodes

105 are investigated, along with their electrochemical performances as stand-alone

106 electrodes or as symmetrical all-solid-state supercapacitor devices.

107

108 2. Experimental work

109 2.1. Materials and reagents

110 Aluminum nitrate nonahydrate ($Al(NO_3)_3.9\ H_2O$, 98%), terephthalic acid (TPA,

111 1,4-benzene dicarboxylic acid, 98%), sodium hydroxide (NaOH, 98%), graphite

112 flakes (<20 μm), sulfuric acid (H_2SO_4), sodium nitrate ($NaNO_3$, 99%), potassium

113 persulfate ($K_2S_2O_8$, 99%) , phosphorus pentoxide (P_2O_5, 99%), hydrochloric acid

114 (HCl, 37%) , hydrogen peroxide (H_2O_2, 35%), pyrrole (C_4H_4NH, 99%), polyvinyl

115 alcohol (PVA, Mw= 89,000-98,000, 99% hydrolyzed) and ferric chloride ($FeCl_3$,

116 98%), L-ascorbic acid ($C_6H_8O_6$, 99%) were all of analytical grade from Sigma-

117 Aldrich Co. Potassium permanganate ($KMnO_4$, 99%) was purchased from ACS

118 Merck Co. All chemicals were used without further purification. Polyethylene

119 terephthalate (PET) woven fabric with plain weave and 15 μm of average fiber

120 diameter, 107 g m^{-2} of weight and 31.5/21.5 cm^{-1} of wrap/weft density, was

121 provided by the Yazdbaf Co. Prior to use, the fabric samples were washed in

122 nonionic detergent solution at 60 °C to remove impurities.

123

124 2.2. Procedures

125 2.2.1. Synthesis of $Al_2(BDC)_3$

126 An aqueous solution of H_2BDC (8 mmol) and sodium hydroxide (16 mmol) in 12

127 mL deionized water (DI) was added dropwise over an aqueous solution (12 mL) of

128 aluminum nitrate nonahydrate (16 mmol) under stirring at room temperature. The

129 stirring was continued for 4 days and then the product was centrifuged, washed and

130 dried in air overnight. Afterwards, the product was activated by DMF as solvent

131 under ultrasonic radiation in 70 °C for 1 h. The purified powder was collected after

132 filtration and dried at 150 °C [24].

133

134 2.2.2. Deposition of $Al_2(BDC)_3$ on the PET fabric

135 The PET fabric was immersed in aqueous solutions of aluminum nitrate

136 nonahydrate, which served as the metal source, for 30 min at room temperature and

137 then washed thoroughly with DI water. After drying at 70 °C, the treated fabric

138 was immersed in sodium terephthalate (Na_2BDC) as the linker salt for 30 min at

139 room temperature and then washed and dried. The same molar ratio was kept

140 during these synthesis steps as those mentioned in section 2.2.1. An excess of

141 sodium hydroxide was used to partially modify the PET surface [25]. It should be

142 noted that the sodium salt of H_2BDC was obtained by the reaction of H_2BDC and

143 NaOH according to the reaction 1 given in [23]. The samples prepared in this way

144 are noted as PET/MOF-1.

8
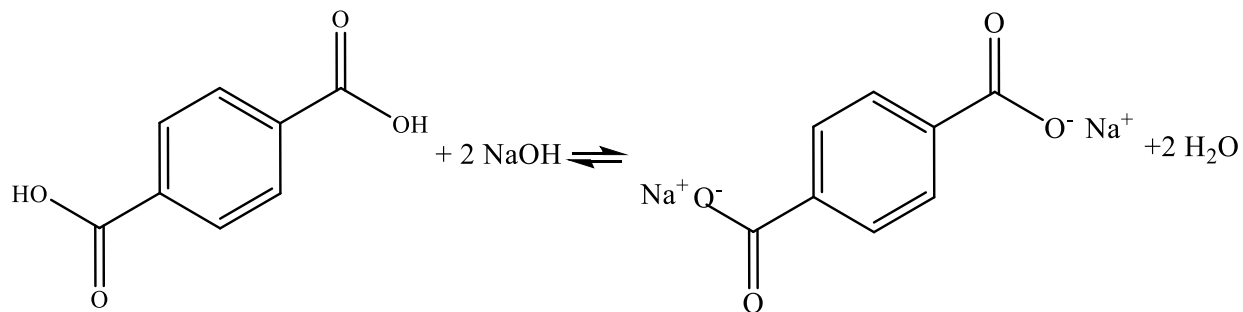
Reaction 1. Reaction of H_2BDC and sodium hydroxide to produce Na_2BDC

The mentioned cycle was repeated 6 times and the obtained samples were named PET/MOF-6.

2.2.3. GO preparation

Prior to GO powder preparation, a pre-oxidation step was carried out according to [20]. Briefly, graphite flakes were added to the hot solution of H_2SO_4, $K_2S_2O_8$ and P_2O_5 and stirred for 4.5 h. The obtained suspensions were diluted with DI water and filtered. Then, the obtained solid was dried in air overnight. GO oxidation was performed via the modified Hummers method [26,27]. The GO dispersion was purified with dialysis for 2 weeks and then it was placed in a vacuum desiccator over phosphorous pentoxide for a week. A solution of 5 mg ml^{-1} of GO was ultra-sonicated for 1 h in order to exfoliate the GO sheets.

9

2.2.4. Preparation of PET/MOF/rGO

The PET/MOF-x samples were soaked in the GO solution at 70 °C for 1 h followed by a thermal treatment at 80 °C. This procedure was repeated 5 times in order to increase the GO loading. The reduction of GO to rGO was carried out in an ascorbic acid solution (100 mM) at 95 °C for 15 min. A few drops of ammonia were added to the solution to maintain the pH around 9-10. After washing and drying at 80 °C for 30 min, the PET/MOF-x/rGO, x=1 or 6, electrodes were prepared.

2.2.5. *In situ* polymerization of pyrrole on PET/MOF/rGO

The PET/MOF-x/rGO samples were immersed in a pyrrole solution (1 M) in an ice bath for 30 min, and then ferric chloride (0.5 M) was poured in the solution. The polymerization time was 2.5 h, and after that, the sample was taken out, washed and dried in ambient conditions. These samples were named PET/MOF-1/rGO/PPy and PET/MOF-6/rGO/PPy.

2.2.6. Fabrication of flexible, symmetric supercapacitor devices

The PET/MOF-x/rGO/PPy strips (1 cm^2) were used directly as electrodes of the supercapacitor device. The gel electrolyte (PVA+H$_2$SO$_4$) was prepared according

178 to [20] and coated on the one side of the electrodes. A cellulosic membrane

179 separator was placed between the electrodes, and the device was pressed overnight

180 under a stainless steel weight (30 g). Finally, the prepared device was dried at room

181 temperature.

182

183 2.3. Characterization

184 The morphologies and composition of the modified PET, the various composites,

185 as well as that of the $Al_2(BDC)_3$ particles were determined by scanning electron

186 microscopy (SEM, Philips XL30) equipped with wavelength dispersive

187 spectroscopy (WDS). Nitrogen sorption measurements were carried out in a

188 BelSorp mini II instrument at 77 K. Prior to measurement, H_2O was removed from

189 the MOF pores by a degasification process [28]. BET areas were extracted by

190 applying the linearized BET equation on the nitrogen adsorption isotherms. The

191 pore size distribution was analyzed by the Barrett-Joyner-Halenda (BJH) method

192 [28]. Fourier Transform Infrared Spectroscopy (FT-IR, Thermo Nicolet Nexus

193 670) was applied to characterize the functional groups of PET/MOF/rGO/PPy. An

194 X-ray diffractometer (Inel, EQUINOX 3000) was used to collect powder x-ray

195 diffraction (XRD) patterns. The air permeability of the samples was investigated

196 by an SDL Atlas air permeability tester. Thermogravimetric analysis (TGA) was

197 performed in a Netzsch STA 449 F1 thermobalance equipped with a SiC furnace

198   up to 900 °C by employing a ramp rate of 10 °C min^{-1} under N_2 gas. The weight of

199   the fabric was recorded before and after each coating. The thicknesses of the

200   composites were also measured by a micrometer in three areas and the mean value

201   was considered as the thickness of each composite. The electrical conductivity of

202   the composites was measured by using a four-point probe method in a BT-112

203   membrane conductivity cell (Scribner Associates, Inc.) and determined according

204   to Eq. (1).

$$\sigma = \frac{s \times I}{E \times w \times t} \qquad\qquad \text{Eq. (1)}$$

205   where σ is electrical conductivity (S cm^{-1}), I the applied current (mA), E the

206   measured voltage (mV), w the width of the sample (1.5 cm), t the thickness (cm),

207   and s the distance between the voltage probes (0.425 cm).

208   In order to characterize the electrochemical performance of the electrodes and

209   devices, cyclic voltammetry (CV), galvanostatic charge-discharge (GCD) and

210   electrochemical impedance spectroscopy (EIS) measurements were conducted in

211   both two- and three-electrode arrangements with a Gamry Reference 3000

212   Potentiostat / Galvanostat / ZRA in which a platinum sheet and a saturated calomel

213   electrode served as counter and reference electrodes, respectively. EIS was

214   recorded at open circuit potential (OCP) in a frequency range from 100 kHz to 0.1

215   Hz and the amplitude of the imposed sinusoidal voltage was 10 mV RMS. The

216   calculated χ-square fitting parameter was of the order of 10^{-4} over the experimental

217   frequency range in all systems.

218   On the subject of the wearable supercapacitors, since only 2 m^2 of a human body is

219   available, attention should be drawn in designing devices offering high areal and

220   volumetric capacitance [29]. The areal capacitance, volumetric capacitance, energy

221   density and power density of the supercapacitor device were calculated according

222   to Eq. (2)-(5).

$$C_{areal} = \frac{\int IdE}{A\upsilon\Delta E}$$ Eq. (2)

$$C_{vol} = \frac{I\Delta t}{V(\Delta E - IR_{drop})}$$ Eq. (3)

$$E_D = \frac{1}{7200}C_{areal}E^2$$ Eq. (4)

$$P_D = \frac{3600E_D}{\Delta t}$$ Eq. (5)

223   Here C_{areal} is the areal capacitance (F cm^{-2}), $\int IdE$ the total charge integrated from

224   CV curves (C V s^{-1}), υ the scan rate (V s^{-1}), ΔE the potential window (V), A the

225   area of the device (cm^2), C_{vol} the volumetric capacitance (F cm^{-3}), I the discharge

226   current (A), Δt the discharge time (s), IR_{drop} the IR voltage drop of the discharge

227   curve (V), *V* the volume of electrodes (cm^{-3}), E_D the energy density (W h cm^{-2}),

228   and P_D the power density (W cm^{-2}).

229

230   3.   Results and discussion

231   Table 1 provides information regarding the mass loading and thickness of the

232   different fabric-composites.

233
234   It may be noticed that by increasing the layer-by-layer assembly cycles from 1 to 6,

235   a substantial increase in the MOF loading onto the PET from 3.3 to 16.4 is

236   observed. Nevertheless, the large MOF loading reduces the amount of rGO and

237   PPy uptake, showing approximately a 3-fold decrease. With respect to the

238   thickness, it can be seen that the thicker electrodes were obtained by the composite

239   prepared from six cycles of MOF deposition. However, the increase in the

240   thickness of the electrodes after PPy loading is proportionally higher in the case of

241   the PET/MOF-1/rGO composites.

242   PET in the MOF precursor solutions containing NaOH is expected to hydrolyze,

243   cleaving a number of ester groups. It occurs according to a nucleophilic attack of

244   the hydroxyl ions to the carbonyl groups of PET [25]. Such surface modification

245   improves the contact between the MOF layer and the PET surface [30]. As stated

246   in Reaction 2, this process introduces reactive carboxylate anions on the surface of

247   PET that are able to bind with Al^{3+} ions via coordination and electrostatic

248   interactions, as shown in Fig.1a [25].

249

250
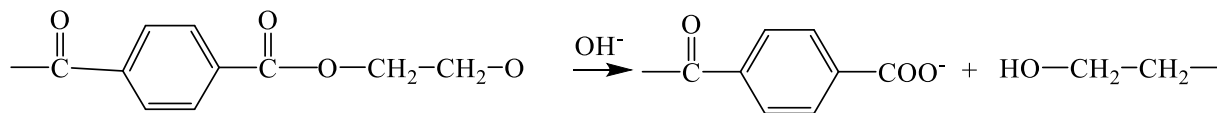
251   Reaction 2. Hydrolysis of PET with NaOH

252

253   The Al^{3+} chelation with the PET functional groups is followed by the coordination

254   of benzene dicarboxylate ions (BDC^{2-}) and the aluminum ions and the growth of

255   $Al_2(BDC)_3$ on the surface and inside the fabric cavities. It is also possible to form a

256   linkage between H_2BDC and carbonyl groups of PET through hydrogen bonding as

257   illustrated in Fig. 1b.

258   Subsequently, upon immersing the PET/MOF in the GO solution, several types of

259   interactions are likely to take place: 1) electrostatic attraction between the metal

260   centers of MOF and the oxygenated functionalities of GO; 2) covalent interaction

261   between the organic molecules of the linker with the sp^2 carbon or oxygenated

262   functional groups of GO [31]; 3) the π-π stacking among the abundant aromatic

263   rings in the MOF (or PET) and the GO [32]. The adhesion of PPy to rGO is also

264   ascribed to π-π stacking as illustrated in Fig. 2.

265

266   3.1.   Chemical structure

3.1.1. XRD

Fig. 3 shows the XRD patterns of the PET, $Al_2(BDC)_3$, PET/MOF, PET/MOF/GO and PET/MOF/rGO/PPy. The X-ray diffraction of $Al_2(BDC)_3$, i.e. the MOF, shows the main peaks at 2θ = 9.6, 10.4, 15.1, 17.5, 20, 23.2, 28.5, 31.9° which are consistent with the pattern of MIL-53(Al) reported previously [22,23]. The untreated PET fabric exhibits three broad diffraction peaks at 2θ=17.5, 22.5 and 26° assigned to (010), (110) and (100) lattice plane of polyethylene terephthalate, respectively (PDF Card # 00-050-2275). The PET/MOF composite displays both the $Al_2(BDC)_3$ and the PET diffraction peaks. This indicates the successful formation of MOF crystals in the composite at room temperature without noticeable change in the PET crystalline structure. For the prepared GO powder, a crystalline phase was detected at 2θ=10.96° corresponding to a d-spacing of 0.8 nm, Fig. S1. This peak is obviously introduced to the PET/MOF/GO at 2θ=11.14° as demonstrated in Fig. 3. In the XRD pattern of the PET/MOF/rGO/PPy, upon reduction and partial removal of the oxygenated functional groups, the GO peak vanishes due to a decrease in the interplanar spacing between the graphitic sheets, therefore the XRD peak shifts towards higher angles. In addition, the XRD peak of PPy overlaps with the broad PET peaks and some weak diffraction peaks of MOF are still detected in the quaternary composite.

286

3.1.2. Infrared Spectroscopy

The IR spectra of the quaternary composite and the PET substrate are compared in Fig. 4 where the characteristic PPy peaks can be seen. The peaks at 788, 1039 and 1176 are assigned to the bending vibration of pyrrole [33]. The peak at 962 cm^{-1} is ascribed to C-C out-of-plane ring deformation mode. The FT-IR peak observed at 1093 cm^{-1} can be related to in-plane deformation of N^{+}-H formed during protonation. The vibrations at 1126 cm^{-1} are ascribed to the C-N stretching. The stretching vibration of the pyrrole ring is also observed at 1542 cm^{-1} [33-35]. It is worth highlighting that the IR spectra of the PET/MOF/rGO/PPy still maintain some weak peaks of the MOF. The absorption band appearing at 1506 cm^{-1} is attributed to stretching vibrations of the carbonyl groups that are coordinated to aluminum [22,36]. A very small peak is also detectable at 1635 cm^{-1} which can possibly be attributed to the free carboxylic groups of unreacted/uncoordinated TPA molecules in the composite, as well as to sp^2 carbon atoms of graphene [22,31]. All these spectroscopic evidence match well with the literature, indicating the successful coating of MOF and PPy on the surface of the PET.

303

3.1.3. BET

305 A crucial property of MOFs is their high specific surface area. The specific surface

306 area of MOF powder prepared at room temperature and purified via ultrasonic

307 radiation was assessed by BET analysis, as shown in Fig. 3a. The N_2 adsorption–

308 desorption isotherm of the RT-prepared $Al_2(BDC)_3$ is typical of a type IV

309 mesoporous materials, according to the IUPAC classification [37]. Moreover, the

310 mesoporous $Al_2(BDC)_3$ provides a specific surface area of 214 m^2 g^{-1} and pores

311 with mean diameter of nearly 10 nm.

312

313 3.1.4. Air permeability test

314 Air permeability is defined as the rate of air flow passing perpendicular through a

315 circular area of 5 cm^2, under a specified air pressure differential between the two

316 surfaces of a material. These measurements were conducted three times in random

317 circular areas of the samples and the mean value is reported here. Fig. 3b depicts

318 the air permeability of the untreated, MOF coated and MOF/rGO/PPy coated

319 fabrics. The air permeability of the raw fabric is almost 15 ml cm^{-2} s^{-1} and reaches

320 31 and 38 after one and six deposition cycles of MOF. This increase suggests the

321 introduction of a new porous material into the primary structure. It should be noted

322 that the slight surface modification of PET has also an influence on its air

323 permeability. The air permeability of the control sample, which was prepared by

324   the use of only NaOH, is 28 ml cm^{-2} s^{-1}. However, the thorough coverage of the

325   PET/MOF surface after the rGO/PPy coating decreases the air permeability to 20

326   and 25 ml cm^{-2} s^{-1} for PET/MOF-1/rGO/PPy and PET/MOF-6/rGO/PPy,

327   respectively, which still satisfies the wearing requirements as the air permeability

328   remains higher than that of the untreated fabric.

329

330   3.1.5. TGA

331   The thermal behavior of the untreated PET, PET/MOF and PET/MOF/rGO/PPy is

332   shown in Fig. 5c. The decomposition of PET is initiated by free radical formation

333   and is further continued by a chain fragmentation process [38]. The thermal

334   stability of PET is improved while is coated with MOF particles. The difference in

335   the final amount of weight loss between PET and PET/MOF is ascribed to the fact

336   that the MOF residue is Al_2O_3. The TG curve of the PET/MOF/rGO/PPy

337   composite is slightly different in the onset of weight loss, below 400 °C. It is likely

338   to be related to the decomposition of epoxy and carboxylic groups remaining even

339   after GO reduction, as well as the degradation of PPy [39,40]. Lastly, the higher

340   proportion of weight remaining at 900 °C for the PET/MOF/rGO/PPy composite is

341   due to the carbon residues of rGO and PPy [39,40].

342

343 3.2.   Morphological study

344 The images of $Al_2(BDC)_3$ particles are displayed in Fig. S2. It can be seen that

345 $Al_2(BDC)_3$ is formed in a particle-like structure with nanometer-scale width.

346 The SEM micrographs of PET/MOF-x and PET/MOF-x/rGO/PPy (x is 1 or 6) are

347 demonstrated in Fig. 6. Fig. 6(a,b) show the PET surface after one cycle of

348 $Al_2(BDC)_3$ deposition. The size of $Al_2(BDC)_3$ is altered upon the synthesis on the

349 fabric surface. Aggregated particles of $Al_2(BDC)_3$ on the PET surface have

350 exhibited varied size ranging from 2.4 to 4.6 μm in PET/MOF-1, whereas in the

351 case of $Al_2(BDC)_3$ powder the mean width of particles reaches up to 75 nm. This is

352 possibly due to the more prolonged reaction time devoted to the synthesis of

353 $Al_2(BDC)_3$ [41] . On the other hand, the sequential deposition cycles in PET/MOF-

354 6 leads to a dense coating according to Fig. 6(c,d). The higher magnification image

355 of PET/MOF-6 reveals that the MOF structures have grown as the smooth facets

356 with the mean width of 112 nm, according to Fig. S3. Multi-point EDX was also

357 employed and showed a strong peak at 1.5 keV corresponding to the Al element, as

358 can be seen in Fig. S4.

359 A glance at the optical images in Fig. S5 shows the difference in MOF-x

360 composites after GO coating and its reduction to rGO. It can be clearly seen that

361 the dark brown color of PET/MOF-1/GO and the black color of PET/MOF-1/rGO

20

362 turns to yellowish-brown and grey for PET/MOF-6/GO and PET/MOF-6/rGO,

363 respectively. The color changes are assigned to the more uptake of GO in the case

364 of the MOF-1 composites.

365 After the loading of active materials of rGO/PPy, a marked contrast is observed

366 for two composites in terms of the amount of coating as well as the uniformity,

367 according Fig. 6(e-h). The higher magnification images of PET/MOF-x/rGO/PPy

368 composites, Fig. 6(f,h) and the corresponding WDX maps, Fig. S6(a,b), reveals

369 that the much higher amount of MOF uptake in PET/MOF-6/rGO/PPy hinders the

370 formation of a uniform and effective coating of active materials. Hence, although

371 in the case of PET/MOF-1/rGO/PPy, a dense and uniform loading is achieved,

372 PET/MOF-6/rGO/PPy experiences the agglomeration of the synthesized particles

373 and consequently the discontinuity of the electro-active species coating.

374

375 3.3.   Electrochemical performance

376 3.3.1. Conductivity Measurements

377 The PET fabric is an electronic insulator. After treatment with MOF, it still

378 remains an insulator since $Al_2(BDC)_3$ is also intrinsically insulating due to the

379 presence of the terephthalate ligands [15]. As indicated in Table 2, introduction of

380 rGO on the PET/MOF-x remarkably increases the electrical conductivity of the

381 non-conductive composite. This is the result of a delocalized flow of electrons

382 within the carbon layers. During the polymerization of the pyrrole, the Fe^{3+} ions

383 are responsible for oxidizing the pyrrole rings, while the Cl^- ions act as counter

384 ions for doping of the polymeric backbone. As a consequence, charge carriers are

385 formed as shown in Reaction 3 [19].
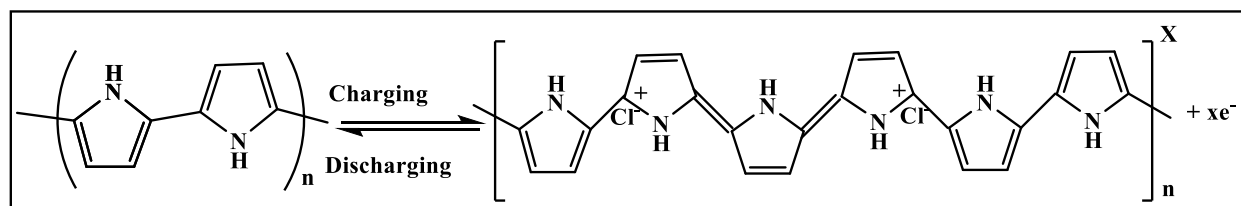
386

387 Reaction 3. Doping/de-doping of PPy

388 According to the Reaction 3, the formed bipolarons accompanied by the π

389 electrons from the pyrrole rings boost the conductivity of the PET/MOF/rGO/PPy

390 composite.

391 Meanwhile the conjugated bonds of PPy and rGO approach each other and a π-π

392 stacking is constructed at their interface [20]. This leads to a tight attachment of the

393 PPy particles to the rGO matrix and thus a conductive network can be established

394 throughout the composite [20]. After the PPy deposition, the conductivity values

395 are greatly enhanced almost four orders of magnitudes for both composites.

396 However, the values for PET/MOF-1/rGO/PPy are almost two times higher than

397 the ones for PET/MOF-6/rGO/PPy. In agreement with the morphological

398 observations, the lower conductivity of the MOF-6 composites is possibly due to

399 the lower mass loading of active materials as well as the blockage of the

400 conduction routes by numerous insulating MOF aggregates. In addition, as a result

401 of the covalent interaction between the MOF and the rGO, the rGO hybridization

402 state alters from sp^2 to sp^3 and consequently the conductivity drops because of the

403 decrease in the mobility of the charge carriers [31].

404 3.3.2. Electrochemical measurements

405 In order to investigate the kinetics of the fabric-based electrodes, the CV response

406 in an aqueous 1 M H_2SO_4 solution at different scan rates was collected for the

407 PET/MOF-x/rGO/PPy composites in a three-electrode cell configuration (Fig.

408 7(a,b)). Evidently, the redox peak regarding PET/MOF-1/rGO/PPy that appeared at

409 1 and 2 mV s^{-1} become invisible at higher scan rates. Since this type of fabric-

410 based electrodes typically follow relatively slow kinetics, the time for ion

411 migration from the electrolyte solution into the composite is not sufficient at fast

412 rates. Hence, electrode polarization occurs due to the ion accumulation at the

413 interface of the electrode/electrolyte. This is why the pseudocapacitance

414 contribution is lost at the faster scan rates [20,42,43]. However, this fabric

415 electrode delivers high capacitances of 510, 350, 230 mF cm^{-2} at scan rates of 1, 2

416 and 5 mV s^{-1}, respectively. Almost similarly, GCD measurements lead to areal

417 capacitances of 520, 410 and 300 mF cm^{-2} at 0.11, 0.15 and 0.28 mA cm^{-2}. In stark

418 contrast, the capacitive response of the PET/MOF-6/rGO/PPy composite is

419 markedly declined, and by slightly increasing the scan rate, the CV curve is heavily

420 distorted. A possible explanation lies in the differences in the thickness of the

421 electrodes, as well as the mass loading of rGO and PPy. According to Table 1, the

422 MOF-6/rGO/PPy film is thicker than the MOF-1/rGO/PPy impeding the diffusion

423 of the electrolyte ions into the electrode. Thus, only the outer active sites of the

424 composite may participate in the charge storage. In addition, the loading mass of

425 the electroactive materials (rGO and PPy) is much lower in case of PET/MOF-

426 6/rGO/PPy, therefore making the capacitive energy storage less efficient.

427 Two symmetrical supercapacitor devices were prepared from these electrodes and

428 the electrochemical performance of the devices was investigated in a two-electrode

429 setup. Fig. 7(c,d) show the CV curves of the PET/MOF-x/rGO/PPy supercapacitor

430 devices at different scan rates. Although the electrode material resistance leads to a

431 deviation from the ideal rectangular response, which is the characteristic of pure

432 carbon electrodes [44], the quasi-rectangular shape points out that a

433 supercapacitive behavior occurs from the electrical double layer capacitance.

434 Furthermore, it is clear that both devices provide faster kinetics when compared to

435 the three-electrode configuration perhaps due to better interactions of the fabric

436 electrodes with the gel electrolyte rather than with the electrolyte solution. The

437 PET/MOF-1/rGO/PPy composite still performs better than the PET/MOF-

438 6/rGO/PPy as the enclosed area in the CV curve is larger for the PET/MOF-

439 1/rGO/PPy. This may be ascribed to the more uniform coverage of the PPy layer

440 on the high surface area of the rGO sheets. The more efficient electrical contact in

441 the PET/MOF-1/rGO/PPy composite results in a higher concentration of active

442 sites, therefore an improved electrochemical performance. As expected, the

443 capacitance calculated in the three-electrode configuration is bigger than the one

444 obtained by the two-electrode arrangement [45]. Fig. 8a provides a comparison

445 between the areal capacitance values of the PET/MOF-1/rGO/PPy and PET/MOF-

446 6/rGO/PPy symmetrical devices. The areal capacitance of the PET/MOF-

447 1/rGO/PPy supercapacitor reaches 150, 130, 90, 70, 60 mF cm^{-2} at 1, 2, 5, 10 and

448 20 mV s^{-1}, respectively. In comparison, the areal capacitances decrease by

449 approximately 1.4 times for the PET/MOF-6/rGO/PPy device.

450 The volumetric capacitance values of the two devices also confirm the superiority

451 of the PET/MOF-1/rGO/PPy (Fig. 8b). The highest volumetric capacitance equals

452 to 3.4 F cm^{-3}, which is obtained at a scan rate of 1 mV s^{-1}. Interestingly, the

453 PET/MOF-6/rGO/PPy supercapacitor is able to deliver a volumetric capacitance as

454 high as 2.4 F cm^{-3}.

455 Discharge curves of the devices at 0.05 mA cm^{-2} indicate that the PET/MOF-

456 1/rGO/PPy composite has a lower voltage loss and a longer discharge time

457 according to Fig. 8c. The smaller voltage drop, which is ascribed to the internal

458 resistance of the electrode, is well matched with the conductivity measurements.

459 As mentioned in section 3.4.1, the PET/MOF-6/rGO/PPy composite suffers from a

460 lower conductivity caused by the high MOF loading. In addition, the possible

461 covalent interactions between MOF aggregates and rGO may cause alterations to

462 the graphene's carbon hybridization. Hence, the PET/MOF-6/rGO/PPy composite

463 fails to form an interconnected network for electron conduction.

464 The maximum values of energy density and power density generated by the

465 PET/MOF-1/rGO/PPy symmetrical supercapacitor are equal to 64 μW h cm^{-3} (2.9

466 μW h cm^{-2}) and 0.6 mW cm^{-3} (0.03 mW cm^{-2}), respectively. These values are

467 comparable with those obtained by MOFs coated on CNT film interconnected by

468 PEDOT-GO [21], MOF/graphene oxide hybrid interconnected with PEDOT [46],

469 and MOF/PPy coated on carbon fibers [13]. Fig. 8e compares the areal energy and

470 power densities of the PET/MOF-1/rGO/PPy symmetrical supercapacitor device

471 with some flexible supercapacitor devices in the literature [46-51].

472 In order to further investigate the electrochemical performance of the

473 supercapacitor devices, EIS was also conducted. The Nyquist plots are given in

474 Fig. 8d, where it can be seen that both devices exhibit a semicircle in the high

475 frequency region followed by a linear line, which is almost parallel to the

476 imaginary axis, in the low frequency domain. The equivalent circuit used to model

477 these devices is composed of five components including R_s, solution resistance,

478 R_{ct}, charge transfer resistance in the interface of electrode/electrolyte, W_z, Warburg

479 impedance for the ionic diffusion, CPE_{dl} and CPE_F, constant phase elements of the

480 double layer capacitance and the faradic capacitance, respectively. The constant

481 phase element represents non-ideal capacitors. The impedance of a CPE is defined

482 by Eq. (6).

$$Z_{CPE} = Q^{-1}(j\omega)^{-n} \qquad\qquad \text{Eq. (6)}$$

483 where ω is the angular frequency, Q represents a capacitive admittance, j is the

484 imaginary operator, and the n displays the degree of ideality of the capacitor (e.g. a

485 non-uniform surface) ($0 \leq n \leq 1$).

486 According to Table 3, a remarkable difference in the electrochemical response of

487 the two devices is observed. The R_s and R_{ct} values of PET/MOF-1/rGO/PPy and

488 PET/MOF-6/rGO/PPy are 184 and 9.5 Ω cm^2, and 232 and 11.1 Ω cm^2,

489 respectively. This may probably be attributed to the difference in the conductivity

490 values of the electrodes, as discussed previously [20,43], as well as to a decreased

491 ionic conductivity due to the use of gel electrolytes. The latter is also related to the

492 increased Warburg resistances, which include the ionic diffusion in the electrolyte

493 and the pores of the electrodes. It is also possible that the microporous structure of

494 the electrodes may have not been efficiently covered by the gel electrolyte, a fact

495 that will be addressed and studied in future works. Moreover, such high R_s values

496 are not uncommon and have been previously reported in other solid-state

497 supercapacitors [52-54]. The uniform and compact coating of rGO/PPy on the

498 PET/MOF substrate that was achieved in the PET/MOF-1/rGO/PPy composite

499 drastically increases the electron conduction in this composite.

500 The superior capacitive response of PET/MOF-1/rGO/PPy can be attributed to

501 three factors: 1) higher loading of the electrically active materials (rGO and PPy),

502 2) effective interactions of the active materials caused by their specific

503 morphology, and 3) partial contribution of the MOF in the EDLC.

504 In addition, the higher amount of the mass transfer diffusion resistance observed in

505 the case of PET/MOF-6/rGO/PPy is possibly due to the limitation of ion diffusion

506 in the thicker electrode by the longer diffusion distances.

507 The stability of the supercapacitor device was assessed after 12 months storage in

508 ambient conditions. The cycling stability of the PET/MOF-1/rGO/PPy symmetrical

509 supercapacitor device was assessed after 1000 VCs at 20 mV s^{-1}. According to Fig.

510 8f, even after 12 months the device possesses capacitance retention of 85%, which

511 is comparable with that reported for a supercapacitor of MOF-coated on CNT

512 interconnected by PEDOT/GO [46].

513 It is a vitally important requirement of wearable devices to render stable

514 performance after mechanical bending. Fig. S7 displays the CV response of

515 PET/MOF-1/rGO/PPy device after bending motions at various angles. The CV

516 curves at 10 mV s^{-1} nearly overlapped indicating almost no loss in capacitance or

517 structure failure. This demonstrates the high flexibility as well as the ability to

518 integrate wearable electronics for PET/MOF-1/rGO/PPy based supercapacitors.

519

520 4. Conclusions

521 $Al_2(BDC)_3$ was introduced on fabric based on PET by a layer-by-layer assembly in

522 order to increase the porosity of the fabric. XRD, air permeability, SEM and TGA

523 measurements confirmed the presence of MOFs on the fabric surface. An

524 electrochemically conductive composite was further achieved by coating the

525 PET/MOF substrate with rGO/PPy. The composite with the lower MOF loading

526 exhibited a higher conductivity due to a higher loading of electrically active

527 materials and thinner electrode configuration. This optimized morphology

528 facilitated the electron transfer and ion migration from the bulk to the electrode

529 interface achieving an energy density of 64 μW h cm^{-3} and a power density of 0.6

mW cm^{-3}. The mentioned characteristics also led to the superior performance in both two- and three-electrode configurations. The symmetrical supercapacitor device made of PET/MOF-1/rGO/PPy electrodes and PVA+H$_2$SO$_4$ electrolyte offers a good cycling stability even after one year storage in ambient conditions, and 85% capacitive retention after 1000 VCs. These results suggest that the MOF modified PET fabric coated with rGO/PPy holds a great potential for wearable, flexible charge storage devices based on non-toxic materials. There is a lot of room for development and this work highlights the fact that optimization of the amounts and blending of the insulating (PET, MOF) with the electrically conducting components (rGO, PPy) should be pursued in future works.

Acknowledgments

References

1. D. P. Dubal, N. R. Chodankar, D. H. Kim, and P. Gomez-Romero, Towards flexible solid-state supercapacitors for smart and wearable electronics. Chem. Soc. Rev. 47 (2018), 2065–2129.
2. C. Sun, X. Li, Z. Cai, and F. Ge, Carbonized cotton fabric in-situ electrodeposition polypyrrole as high-performance flexible electrode for wearable supercapacitor. Electrochim. Acta 296 (2019), 617-626.
3. P. Simon, Y. Gogotsi, B. Dunn, Where do batteries end and supercapacitors begin? Science 343 (2014), 1210-1211.

4. C. Portet, *et al*., High power density electrodes for carbon supercapacitor applications. Electrochim. Acta 50 (2005), 4174-4181.

5. S. Petnikota, *et al*., Electrochemistry-related aspects of safety of graphene-based non-aqueous electrochemical supercapacitors: a case study with MgO-decorated few-layer graphene as an electrode material, New J. Chem. 43 (2019), 9793-9801.

6. S. G. Krishnan, *et al*., Characterization of MgCo2O4as an electrode for high performance Supercapacitors, Electrochim. Acta 161 (2015), 312–321.

7. S. Sundriyal, *et al*., Metal-organic frameworks and their composites as efficient electrodes for supercapacitor applications. Coordin. Chem. Rev. 369 (2018), 15–38.

8. K. M. Choi, *et al*., Supercapacitors of nanocrystalline metal–organic frameworks. ACS Nano 8 (2014), 7451–7457.

9. G. Xu, *et al*., Exploring metal organic frameworks for energy storage in batteries and supercapacitors. Mater. Today 20 (2017), 191–209.

10. R. Ramachandran, *et al.,* Morphology-dependent electrochemical properties of cobalt-based metal organic frameworks for supercapacitor electrode materials. Electrochim. Acta 267 (2018), 170-180.

11. L. Wang, *et al*., Metal–organic frameworks for energy storage: Batteries and supercapacitors. Coordin. Chem. Rev 307 (2016), 361–381.

12. B. Dhara, *et al*., Increase in electrical conductivity of MOF to billion-fold upon filling the nanochannels with conducting polymer. J. Phys. Chem. Lett. 7 (2016), 2945–2950.

13. K. Qi, *et al*., Construction of Metal–Organic Framework/conductive polymer hybrid for all-solid-state fabric supercapacitor. ACS Appl. Mater. Interfaces 10 (2018), 18021–18028.

14. M. Nagarathinam, *et al*., Redox-active metal-centered oxalato phosphate open framework cathode materials for lithium ion batteries, Angew. Chem. Int. Ed. 51 (2012), 1– 6.

15. L. Wang, *et al*., Flexible solid-state supercapacitor based on a Metal–Organic Framework interwoven by electrochemically-deposited PANI. J. Am. Chem. Soc. 137 (2015), 4920–4923.

16. L. Shao, *et al.*, A high-capacitance flexible solid-state supercapacitor based on polyaniline and Metal-Organic Framework (UiO-66) composites. J. of Power Sources 379 (2018), 350–361.

17. X. Xu, *et al.*, Three-dimensional networked Metal–Organic Frameworks with conductive polypyrrole tubes for flexible supercapacitors. ACS Appl. Mater. Interfaces 9 (2017), 38737–38744.

18. Q. Wang, Hierarchical porous PANI/MIL-101 nanocomposites based solid-state flexible supercapacitor, Electrochim. Acta 281 (2018), 582-593.

19. G.A. Snook, P. Kao, A.S. Best, Conducting-polymer-based supercapacitor devices and electrodes, J. Power Sources 196 (2011) 1-12.

20. M. Barakzehi, M. Montazer, F. Sharif, T. Norby, and A. A. Chatzitakis, A textile-based wearable supercapacitor using reduced graphene oxide/polypyrrole composite. Electrochim. Acta 305(2019), 187–196.

21. D. Fu, *et al.*, Flexible solid-state supercapacitor fabricated by metal-organic framework/graphene oxide hybrid interconnected with PEDOT. Mater. Chem. Phys. 179 (2016), 166–173.

22. T. Loiseau, *et al.*, A rationale for the large breathing of the porous aluminum terephthalate (MIL-53) upon hydration. Chem-Eur. J. 10 (2004), 1373–1382.

23. M. Sánchez-Sánchez, *et al.*, Synthesis of metal–organic frameworks in water at room temperature: salts as linker sources. Green Chem. 17 (2015). 1500–1509.

24. E. Haque, N. A. Khan, J. E. Lee, and S. H. Jhung, Facile purification of porous Metal Terephthalates with ultrasonic treatment in the presence of amides. Chem-Eur. J. 15 (2009), 11730–11736.

25. M. Montazer, and T. Harifi, Nanofinishing of Textile Materials, section 5: Nanosurface activation. Woodhead Publishing, 65-82, (2018), ISBN 9780081012147.

26. W.S. Hummers, R.E. Offeman, Preparation of graphitic oxide, J. Am. Chem. Soc. 80 (1958), 1339-1339.

27. W. Gao, L. B. Alemany, L. Ci, P.M. Ajayan, New insights into the structure and reduction of graphite oxide. Nat. Chem. 1(2009), 403–408.

28. G. C. Shearer, *et al*., Defect engineering: tuning the porosity and composition of the Metal–Organic Framework UiO-66 via modulated synthesis. Chem. Mater. 28(11) (2016), 3749-3761.

29. Y. Yang *et al*., Waterproof, ultrahigh areal-Capacitance, wearable supercapacitor fabrics. Adv. Mater. 29 (2017), 1606679.

30. M. Meilikhov *et al*., Stepwise deposition of metal organic frameworks on flexible synthetic polymer surfaces. Dalton Trans. 40 (2011), 4838–4841.

31. P. Karthik, *et al*., π–π interaction between Metal–Organic Framework and reduced graphene oxide for visible-light photocatalytic H_2 production. ACS Appl. Energy Mater. 1 (2018), 1913–1923.

32. W.K. Chee, H. N. Lim, N. M. Huang, I. Harrison, Nanocomposites of graphene/polymers: a review, RSC Adv. 5 (2015) 68014-68051.

33. J. Molina, *et al*., Conducting fabrics of polyester coated with polypyrrole and doped with graphene oxide, Synthetic Met. 204 (2015) 110-121.

34. M. Devi, A. Kumar, In-situ reduced graphene oxide nanosheets /polypyrrole nanotubes nanocomposites for supercapacitor applications, Synthetic Met. 222 (2016) 318-329.

35. P. Pattananuwat, D. Aht-ong, Controllable morphology of polypyrrole wrapped graphene hydrogel framework composites via cyclic voltammetry with aiding of poly (sodium 4-styrene sulfonate) for the flexible supercapacitor electrode, Electrochim. Acta 224 (2017) 149-160.

36. W. P. Mounfield, and K. S. Walton, Effect of synthesis solvent on the breathing behavior of MIL-53(Al), J. Colloid Interf. Sci. 447(2015), 33–39.

37. J. Rouquerol, Recommendations for the characterization of porous solids, Pure Appl. Chem., 66(1994), 1739– 1758.

38. F. Bertini, and V. V. Zuev, Thermal behaviour and degradation of a liquid crystalline alkylene-aromatic polyester: Poly(decamethylene-fumaroyl-bis-4-oxybenzoate). Polym. Degrad. Stabil. 92(2007), 1669–1676.

39. S. Castarlenas, C. Téllez, and J. Coronas, Gas separation with mixed matrix membranes obtained from MOF UiO-66-graphite oxide hybrids. Journal of Membrane Sci. 526 (2017), 205–211.

40. A. Batool, F. Kanwal, M. Imran, T. Jamil, S. A. Siddiqi, Synthesis of polypyrrole/zinc oxide composites and study of their structural, thermal and electrical properties. Synthetic Met. 161(2012), 2753–2758.

41. L. Lu, *et al*., Multi-functional finishing of cotton fabrics by water-based layer-by-layer assembly of metal–organic framework, Cellulose, 25(2018), 4223–4238.

42. Q. Zhou, X. Ye, Z. Wan, C. Jia, A three-dimensional flexible supercapacitor with enhanced performance based on lightweight, conductive graphene-cotton fabric electrode, J. Power Sources 296 (2015), 186-196.

43. J. Xu, *et al*., Polypyrrole/reduced graphene oxide coated fabric electrodes for supercapacitor application, Org. Electron. 24 (2015), 153-159.

44. H. H. Chang, C. K. Chang, Y. C. Tsai, and C. S. Liao, Electrochemically synthesized graphene/polypyrrole composites and their use in supercapacitor. Carbon 50 (2012), 2331–2336.

45. M. D. Stoller, and R. S. Ruoff, Best practice methods for determining an electrode material's performance for ultracapacitors, Energy Environ. Sci. 3(9) (2010), 1294–1301.

46. D. Fu, *et al*., Flexible solid–state supercapacitor of metal–organic framework coated on carbon nanotube film interconnected by electrochemically-codeposited PEDOT-GO. ChemistrySelect 1(2016), 285–289.

47. Q. Meng, *et al*., Thread-like supercapacitors based on one-step spun nanocomposite yarns, Small 10 (2014), 3187-3193.

48. L. Kou, *et al*., Coaxial wet-spun yarn supercapacitors for high-energy density and safe wearable electronics, Nat. Commun. 5 (2014), 3754.

49. Meng, Y. *et al*. All-graphene core-sheath microfibers for all-solid-state, stretchable fibriform supercapacitors and wearable electronic textiles. Adv. Mater. 25 (2013), 2326–2331.

50. X. Pu, *et al*., Wearable self-charging power textile based on flexible yarn supercapacitors and fabric nanogenerators, Adv. Mater. 28 (2016), 98-105.

51. Y.J. Kang, Y. Yoo, W. Kim, 3-V solid-state flexible supercapacitors with ionic liquid-based polymer gel electrolyte for AC line filtering, ACS Appl. Mater. Interfaces 8 (2016), 13909-13917.

669   52. W. Si, *et al*., On chip, all solid-state and flexible micro-supercapacitors with high
670   performance based on MnOx/Au multilayers, Energy environ. Sci., 6 (2013), 3218-3223.
671   53. K. Wang, *et al*., An all-solid-state flexible micro-supercapacitor on a chip, Adv. Energy
672   Mater. 1 (2011), 1068-1072.
673   54. C. Zhang, *et al*., Transparent, flexible and conductive 2D titanium carbide (MXene) films
674   with high volumetric capacitance, Adv. Mater. 29 (2017), 1702678.
675

676 **Figures Captions**

677 Fig. 1. Scheme for the possible interactions to form PET/MOF: (a) interactions of Al^{3+} with the

678 carboxylate groups of the modified PET and the BDC^{-2} anions, and/or (b) interactions of H_2BDC

679 with the modified PET and Al^{3+}

680 Fig. 2. Schematic representation of the preparation of the PET/MOF/rGO/PPy composites

681 Fig. 3. XRD patterns of MOF, PET, PET/MOF, PET/MOF/GO, and PET/MOF/rGO

682 Fig. 4. FTIR spectra of the untreated and PET/MOF/rGO/PPy fabrics. The green, cyan and
683 magenta stars are attributed to PPy, MOF and rGO, respectively.

684 Fig. 5. a) N_2 adsorption/desorption isotherms of $Al_2(BDC)_3$, b) The amount of air permeability of

685 various fabric-based composites, c) TGA curves of the untreated PET, PET/MOF and

686 PET/MOF/rGO/PPy

687 Fig. 6. The SEM images of a,b) PET/MOF-1, c,d) PET/MOF-6 is the higher magnification

688 image, e,f) PET/MOF-1/rGO/PPy, g,h) PET/MOF-6/rGO/PPy

689 Fig. 7. Cyclic voltammograms for a) PET/MOF-1/rGO/PPy electrode b) PET/MOF-6/rGO/PPy

690 electrode in aqueous 1 M H_2SO_4, c) PET/MOF-1/rGO/PPy symmetrical supercapacitor device,

691 and d) PET/MOF-6/rGO/PPy symmetrical supercapacitor device

692 Fig. 8. a) The areal capacitance values and b) the volumetric capacitance values of PET/MOF-

693 1/rGO/PPy and PET/MOF-2/rGO/PPy supercapacitors obtained at different scan rates, c)

694 comparison of discharge curves of PET/MOF-1/rGO/PPy and PET/MOF-6/rGO/PPy

695 supercapacitors at a current density of 0.05 mA cm^{-2}, d) Nyquist plots of PET/MOF-1/rGO/PPy

696 and PET/MOF-6/rGO/PPy devices, e) the Ragone plot, f) capacitance retention of PET/MOF-

697   1/rGO/PPy after 1500 cycles of CV at scan rate of 20 mV s^{-1} after one year storage at ambient

698   conditions

699

700　　**Tables Captions**

701　　Table 1. The weight and thickness of the various composites

702　　Table 2. Conductivity of various composites

703　　Table 3. Extracted EIS parameters after deconvolution of the experimental data

704

705
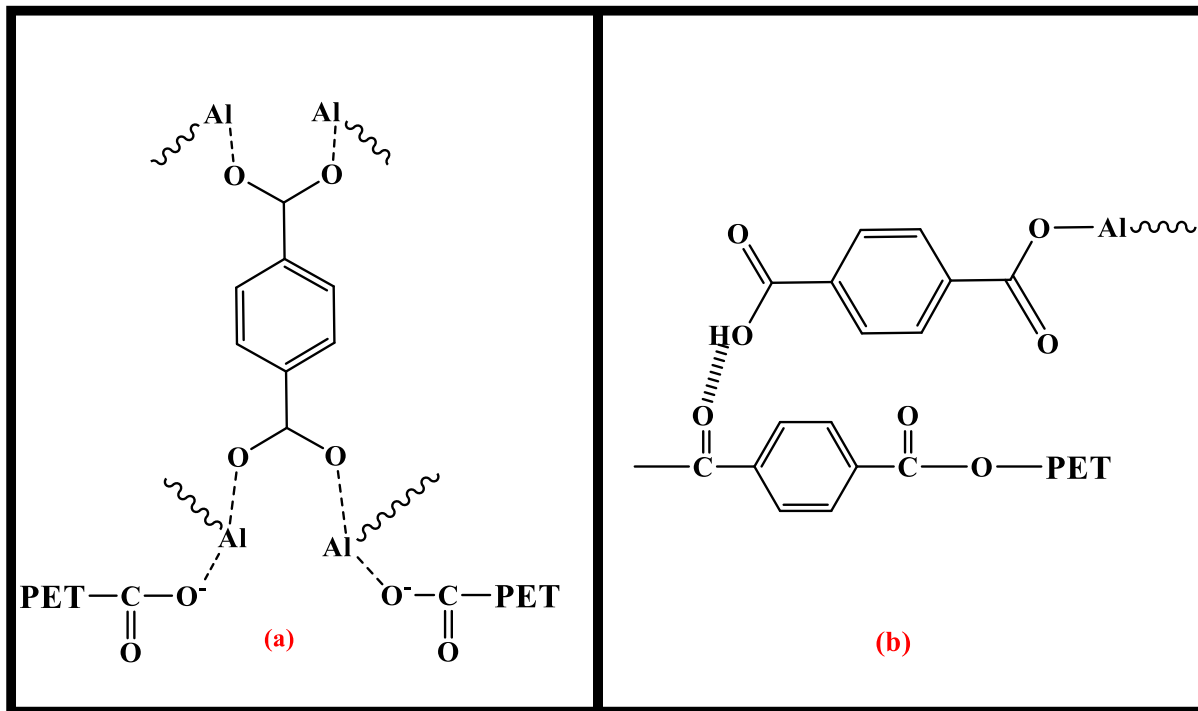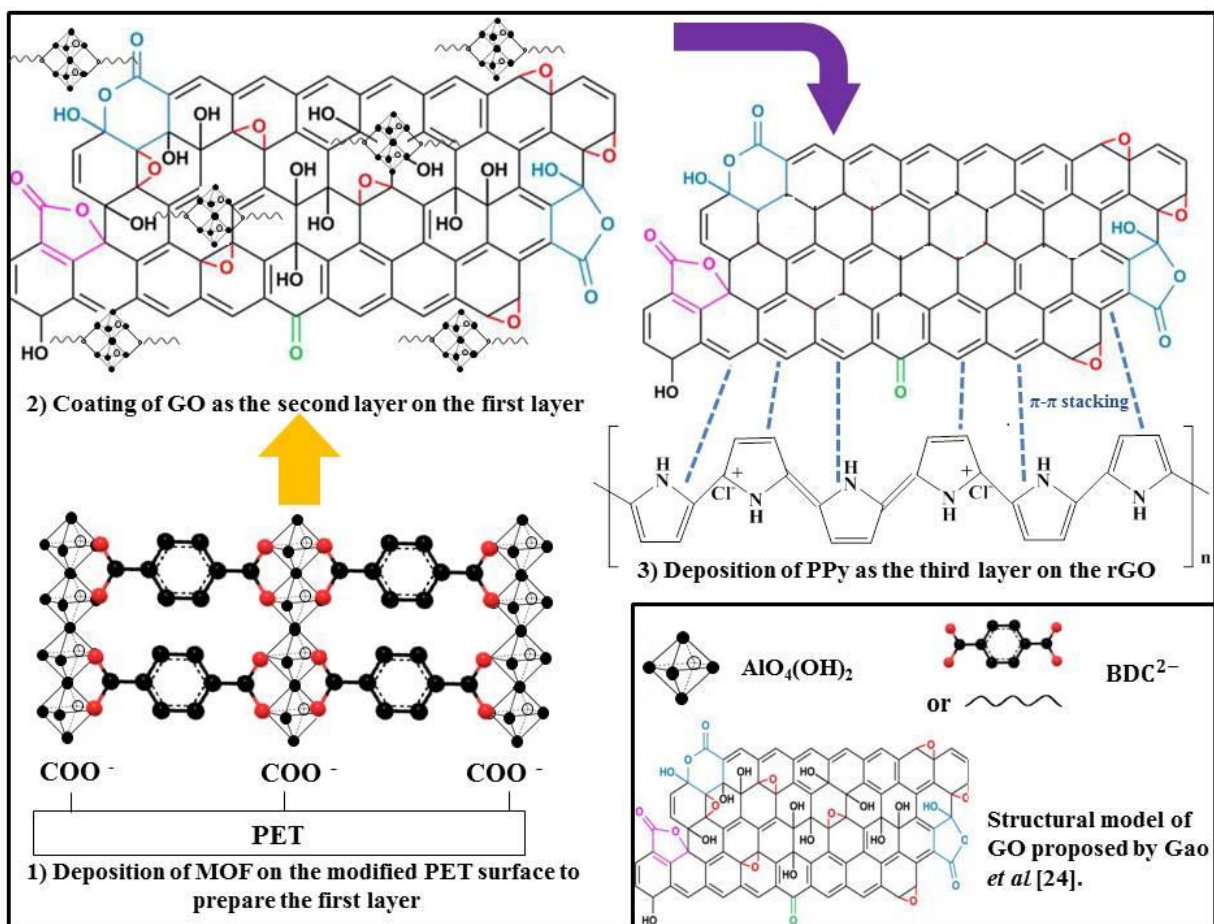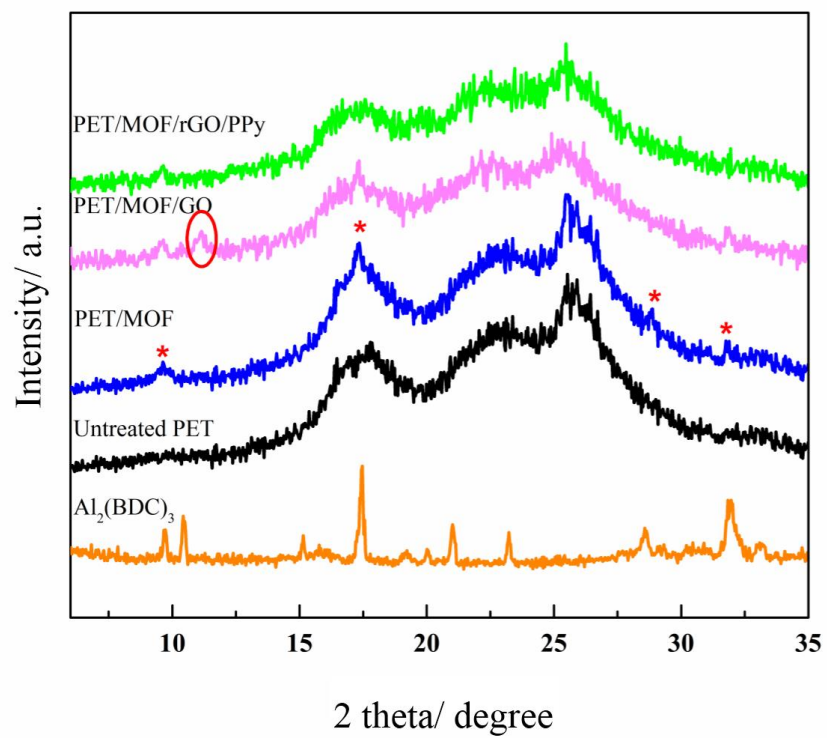
(a)

(b)

Fig. 1

706

707

708

2) Coating of GO as the second layer on the first layer

3) Deposition of PPy as the third layer on the rGO

1) Deposition of MOF on the modified PET surface to prepare the first layer

$AlO_4(OH)_2$

BDC^{2-}

or

Structural model of GO proposed by Gao et al [24].

π-π stacking

COO⁻   COO⁻   COO⁻

PET

709
710   Fig. 2

711

40

712

Fig. 3

713

714

715

716

Fig. 4

717

718

719

a

b

c

Fig. 5

722

45

g

h

723

Fig. 6

724

725

a
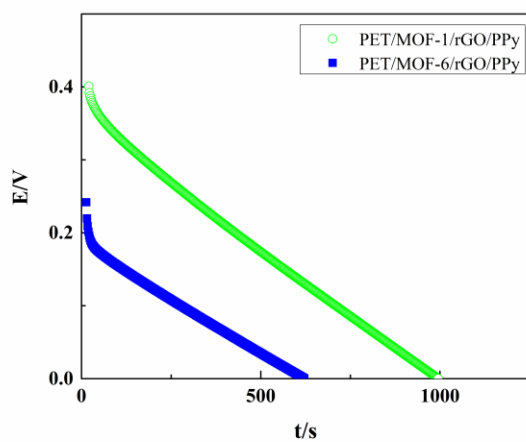
b

c

d

Fig.7

726
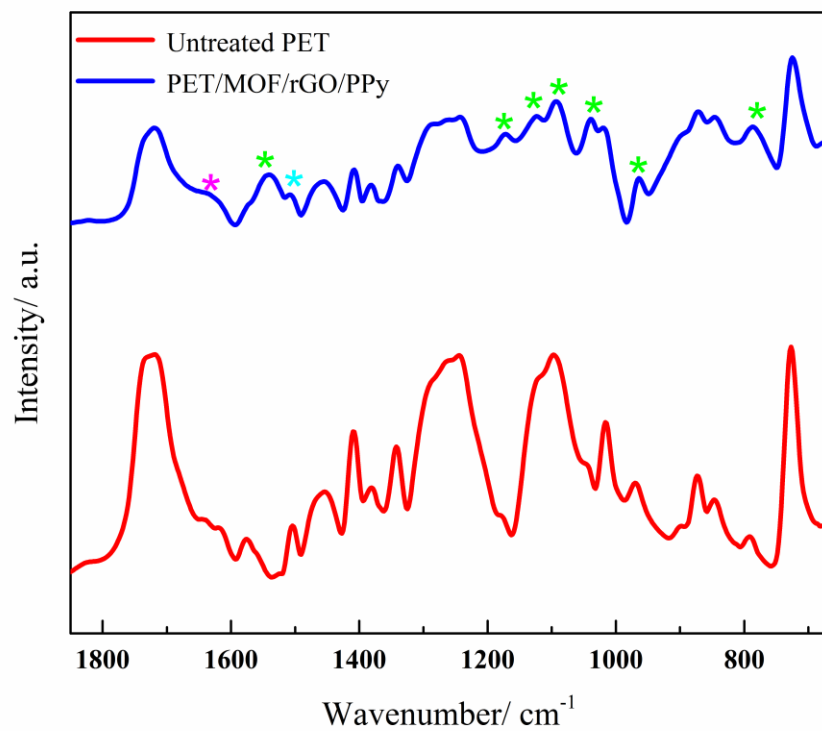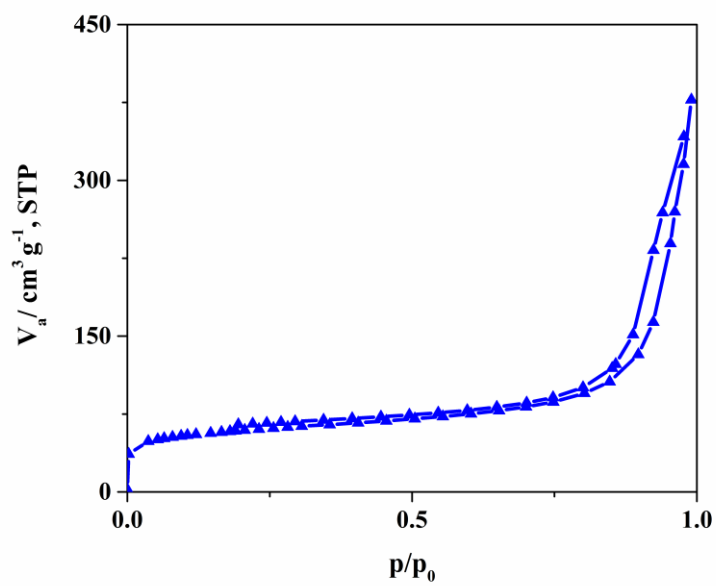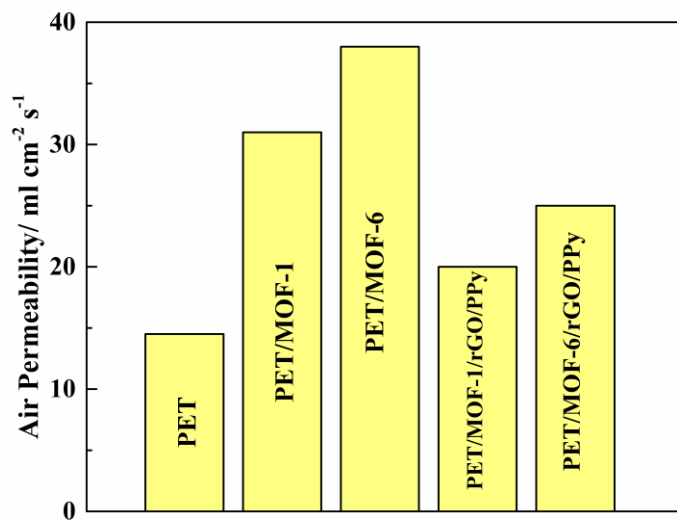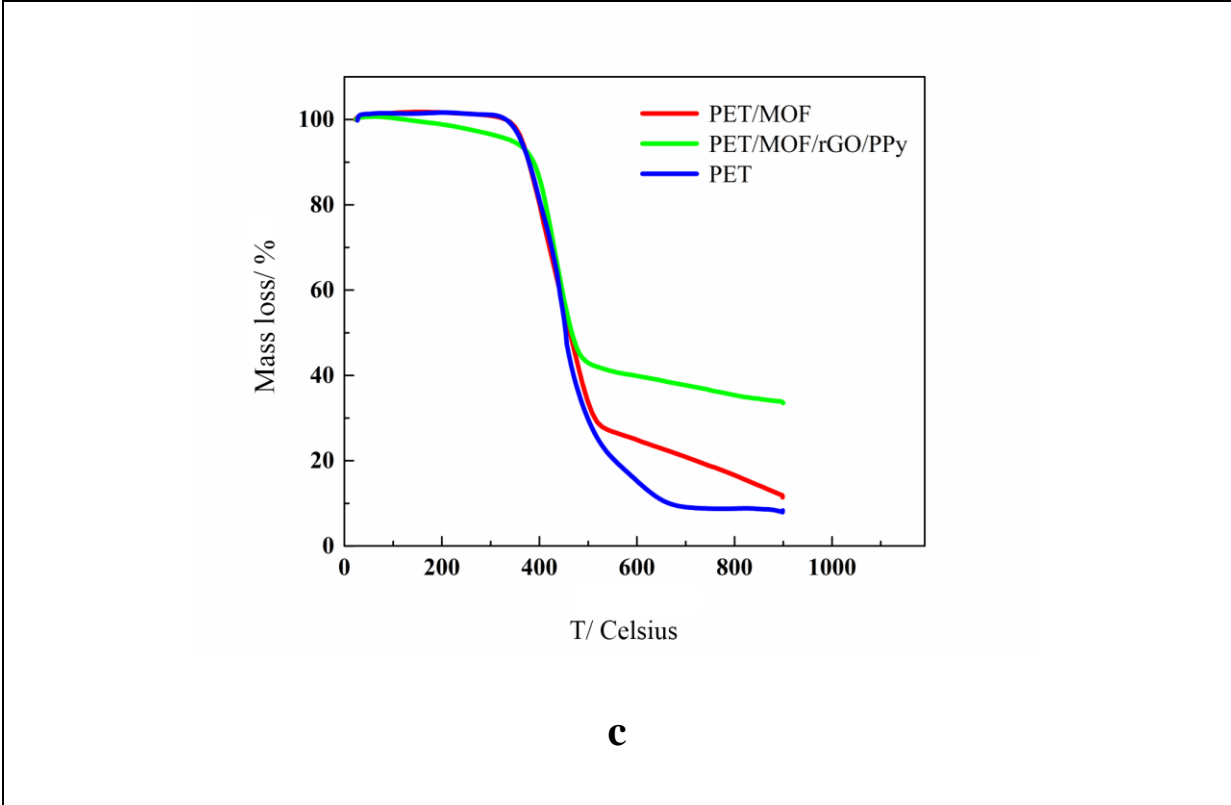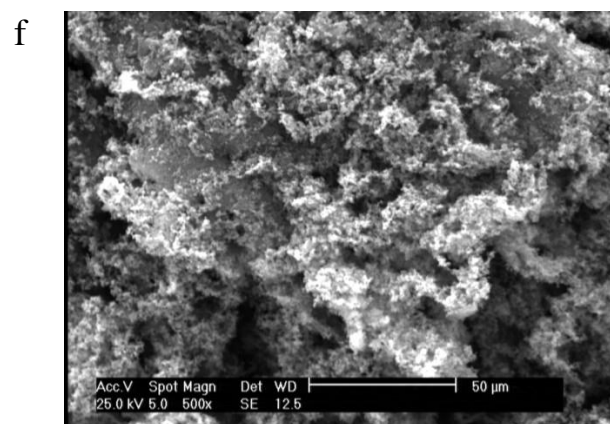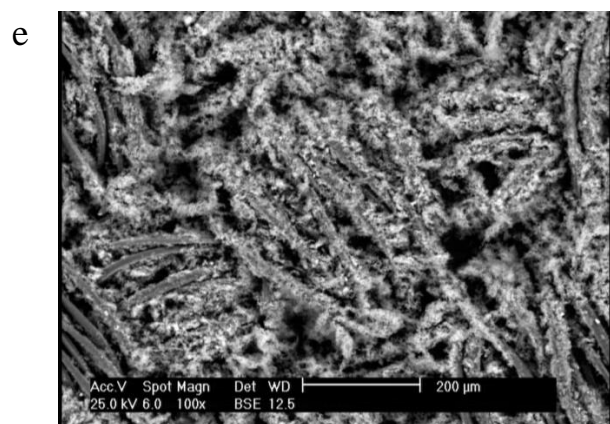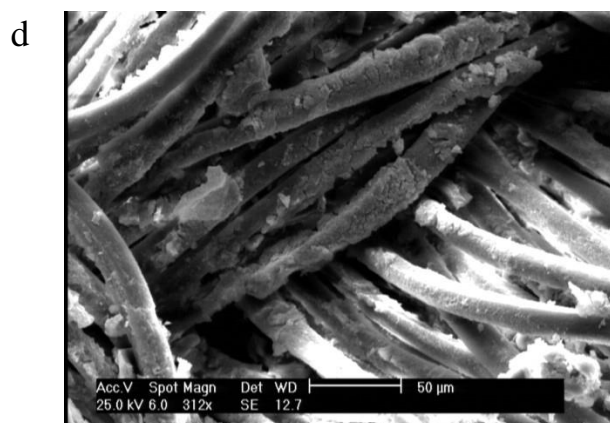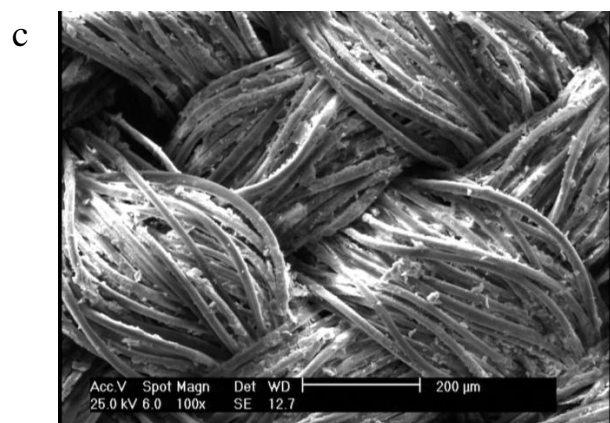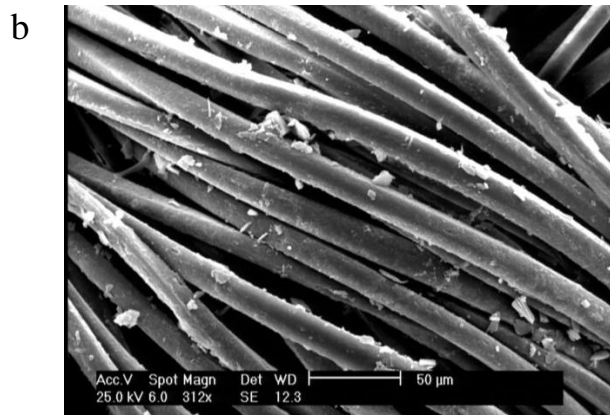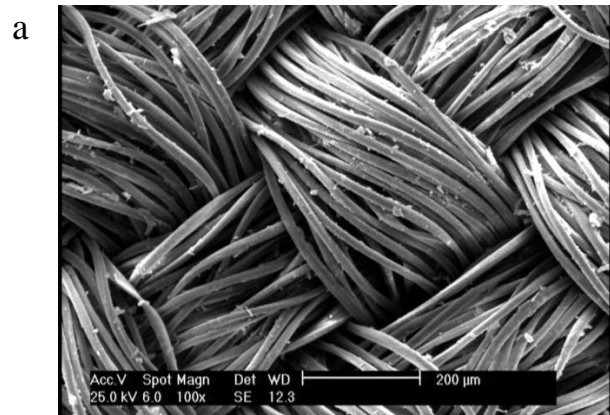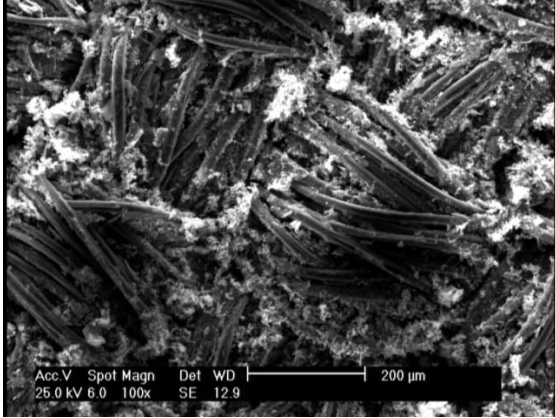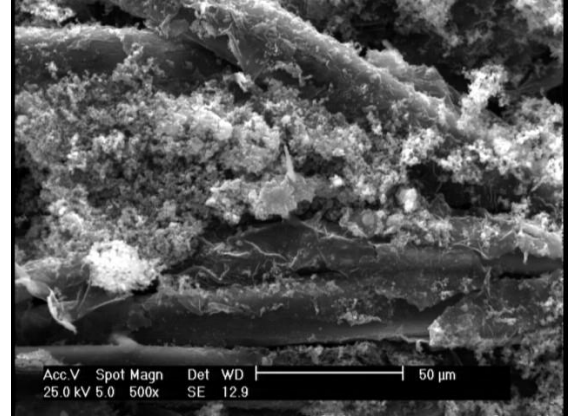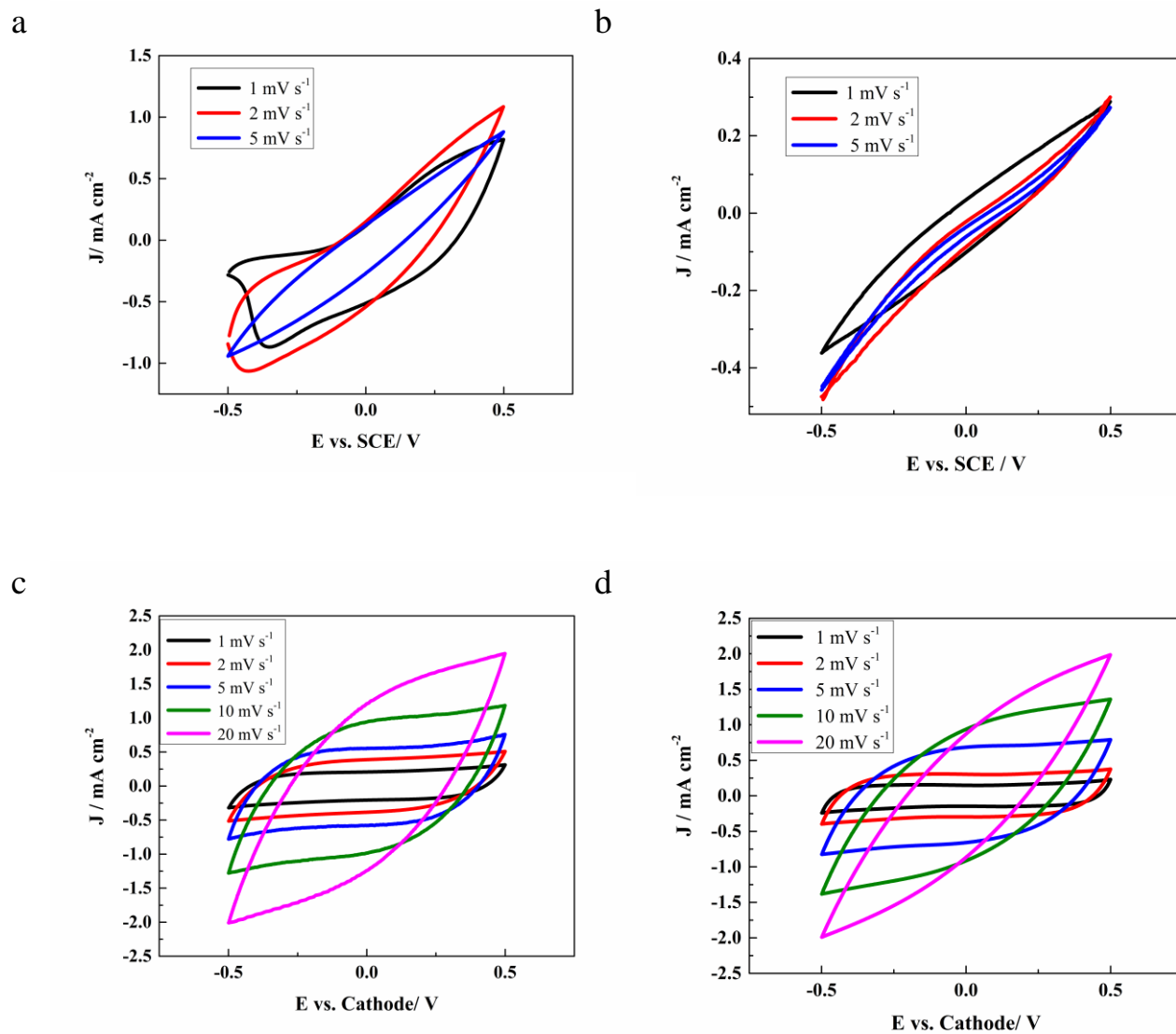
727

a

b

c

d

e

f

729

Fig. 8

730

49
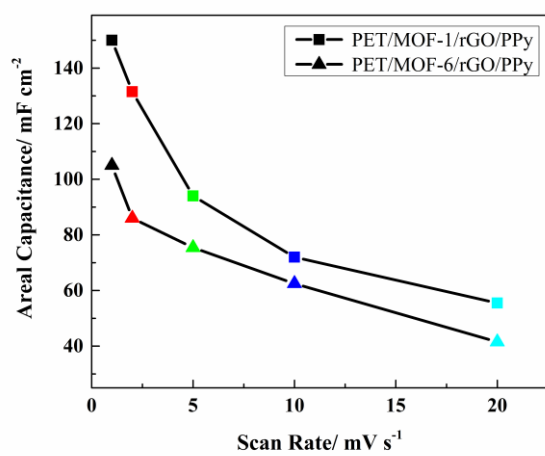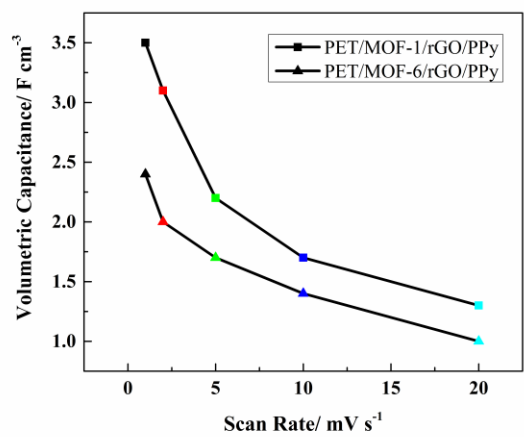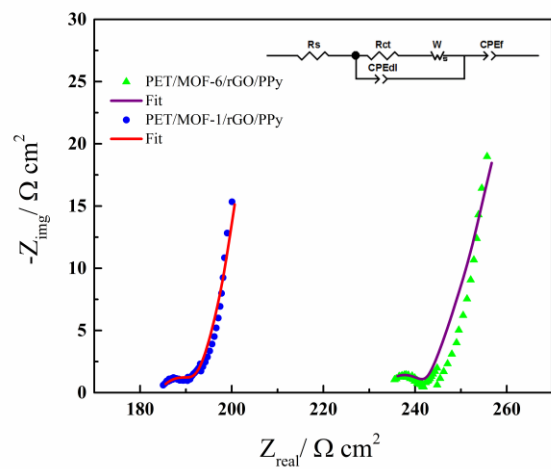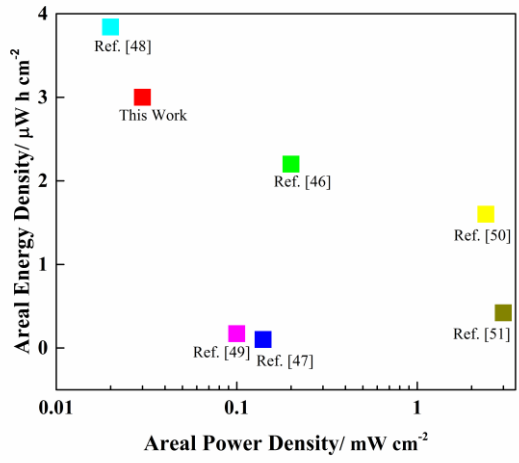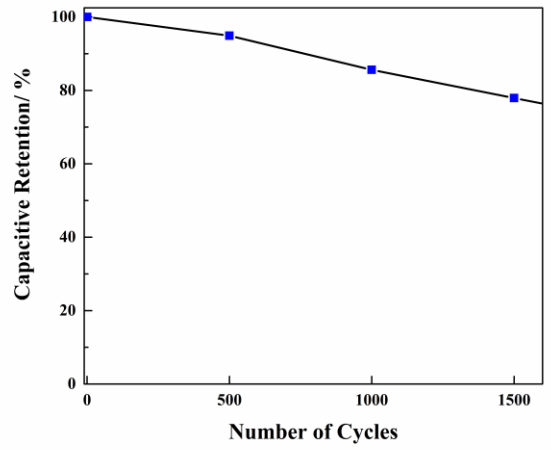
731   Table 1

Composite	Add-on/mg cm^{-2}	Thickness/mm
Untreated PET	-	0.11
PET/MOF-1	3.3	0.12
PET/MOF-1/rGO	5.0	0.13
PET/MOF-1/rGO/PPy	6.2	0.16
PET/MOF-6	16.4	0.15
PET/MOF-6/rGO	1.5	0.16
PET/MOF-6/rGO/PPy	2.4	0.17

732

733

734

Table 2

Composite	Electrical Conductivity/S cm^{-1}
PET/MOF-1/rGO	5.1×10^{-4}
PET/MOF-1/rGO/PPy	0.68
PET/MOF-6/rGO	1.7×10^{-4}
PET/MOF-6/rGO/PPy	0.35

735

Table 3

Device	$R_s/$ $\Omega\ cm^2$	$R_{ct}/$ $\Omega\ cm^2$	$W_R/$ $\Omega\ cm^2$	$CPE_F/$ $F\ cm^{-2}$ $s^{n_{Dl}-1}$	n_F	$CPE_{DL}/$ $F\ cm^{-2}$ s^{n_F-1}	n_{DL}	χ-square
PET/MOF-1/rGO/PPy	184	9.5	47.7	0.0077	0.31	0.25	1	2.5E-4
PET/MOF-6/rGO/PPy	232	11.1	60	0.0021	0.32	0.44	1	1.1E-3

737

738

739

740

741

742

743

744

745

746